

Dojo: A Differentiable Physics Engine for Robotics

Taylor A. Howell*

Department of Mechanical Engineering
Stanford University
thowell@stanford.edu

Simon Le Cleac'h*

Department of Mechanical Engineering
Stanford University
simonlc@stanford.edu

J. Zico Kolter

Department of Computer Science
Carnegie Mellon University
zkolter@cs.cmu.edu

Mac Schwager

Aeronautics and Astronautics Department
Stanford University
schwager@stanford.edu

Zachary Manchester

The Robotics Institute
Carnegie Mellon University
zacm@cmu.edu

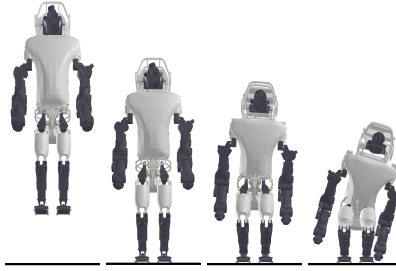


Figure 1: Atlas drop simulation. Dojo simulates this system with 403 maximal-coordinates states, 30 joint constraints, 36 inputs, and 8 contact points in real-time at 65 Hz. Dojo respects floor-feet penetration constraints to machine precision, while MuJoCo suffers from centimeters of interpenetration and is unstable at such low simulation rates.

Abstract: We present Dojo, a differentiable physics engine for robotics that prioritizes stable simulation, accurate contact physics, and differentiability with respect to states, actions, and system parameters. Dojo achieves stable simulation at low sample rates and conserves energy and momentum by employing a variational integrator. A nonlinear complementarity problem, with second-order cones for friction, models hard contact and is reliably solved using a custom primal-dual interior-point method. Special properties of the interior-point method are exploited using the implicit-function theorem to efficiently compute smooth gradients that provide useful information through contact events. We demonstrate Dojo’s unique ability to simulate hard contact while providing smooth, analytic gradients with a number of examples, including trajectory optimization, reinforcement learning, and system identification.

Keywords: contact dynamics, differentiable optimization, simulation

1 Introduction

The last decade has seen immense resources devoted to network architectures, optimization algorithms, and the construction of large datasets by the learning community. These efforts have been leveraged to make impressive advances in robotics including: dexterous manipulation [1, 2], quadrupedal locomotion [3, 4], and pixels-to-torques control [5]. In contrast, there has been comparatively little work on the lowest level of the robotics reinforcement-learning stack: the *physics*

*These authors contributed equally to this work

Table 1: Comparison of popular physics engines for robotics.

engine	application	integrator	state	contact	solver	gradients
MuJoCo	robotics	implicit	minimal	soft	Newton	finite-difference
Drake	robotics	implicit Euler	minimal	soft/hard	LCP	gradient-bundle
Bullet	graphics	implicit Euler	minimal	soft/hard	LCP	sub-gradient
DART	robotics	implicit Euler	minimal	hard	LCP	sub-gradient
PhysX	graphics	explicit	minimal	soft	iterative	finite-difference
Brax	graphics	explicit	maximal	soft	iterative	sub-gradient
Dojo	robotics	variational	maximal	hard	NCP	implicit gradient

engine. We argue that deficiencies in current widely used physics engines form a key bottleneck that must be overcome to enable future advancements in robotics.

Physics engines that simulate rigid-body dynamics with contact are utilized for trajectory optimization, reinforcement learning, system identification, and dataset generation for domains ranging from locomotion to manipulation. To overcome the sim-to-real gap and to be of practical value in real-world applications, an engine should provide stable simulation, accurately emulate a robot’s dynamics, and ideally, be differentiable to enable use of efficient gradient-based optimization methods.

In recent years, a number of physics engines [6, 7, 8, 9, 10, 11] have been developed and utilized for robotics. In this work, we address key deficiencies of these tools including: high sample rates required for stable simulation that exacerbate the vanishing/exploding gradient problem and substantially increase sample complexities for rollout-based optimization methods, interpenetration of rigid bodies (e.g., a robot foot sinking through the floor) or creep (e.g., objects that should be at rest incorrectly sliding), and lack of informative gradients through contact events (e.g., subgradients resulting from naive differentiation of non-smooth dynamics) or expensive gradients that require a large number of calls to the engine (e.g. finite-difference or stochastic-sampling schemes).

The Dojo physics engine is designed from the ground up to enable better and easier optimization for motion planning, control, reinforcement learning, system identification, and high-quality dataset generation. By taking a physics- and optimization-first approach to physics-engine design, we significantly advance the state of the art in *stable simulation, accurate contact physics, and differentiability* for robot simulation. Key attributes of Dojo include:

- Variational integration for stable simulation that is not sensitive to timestep size
- A nonlinear complementarity problem (NCP) model for accurate contact dynamics
- A custom primal-dual interior-point method for reliably solving the NCP
- Smooth, analytic gradients through contact efficiently computed by applying the implicit-function theorem to the interior-point NCP solver

These improvements over current physics engines have important implications for control and reinforcement learning in robotics, including: a substantial reduction in the number of samples required for fixed-horizon rollouts—we demonstrate a 5 times decrease in physics-engine evaluations for numerous scenarios; smooth analytical gradients that are significantly less expensive to compute compared to sampling schemes and enable efficient optimization, reducing the number of samples required for policy training by an order-of-magnitude compared to gradient-free methods; and elimination of interpenetration between rigid bodies and friction artifacts, which should enable improved sim-to-real transfer.

In the remainder of this paper, we first provide an overview of related state-of-the-art physics engines in Section 2. We then summarize important technical background in Section 3. Next, we present Dojo, and its key features, in Section 4. Simulation, trajectory optimization, reinforcement learning, and system identification examples are presented in Section 5. Finally, we discuss Dojo’s limitations in Section 6 and provide closing remarks in Section 7.

2 Existing State-of-the-Art

This section provides an overview of physics engines that are commonly used in robotics. Table 1 summarizes the features of these tools and compares them to Dojo.

Table 2: Contact violation for Atlas drop. Comparison between Dojo and MuJoCo for foot contact penetration (millimeters) with the floor for different time steps h (seconds). Dojo strictly enforces no penetration. When Atlas lands, its feet remains above the ground by an infinitesimal amount. In contrast, MuJoCo exhibits significant penetration through the floor (i.e., negative values).

h	0.1	0.01	0.001
MuJoCo	failure	-28	-46
Dojo	+1e-12	+1e-7	+8e-6

In the learning community, MuJoCo [12] has become a standard for benchmarking reinforcement-learning algorithms using the OpenAI Gym environments [13]. MuJoCo makes a number of approximations to the dynamics and utilizes a soft contact model in order to realize invertible dynamics and simulate systems at high sample rates. Additionally, simulation steps are typically computed approximately using Newton’s method. Unfortunately, these modeling and design choices result in poor simulation stability at low sample rates and inaccurate physical artifacts like interpenetration and creep [14]. Analytical gradients are not provided by the engine, requiring finite-difference schemes that are computationally expensive.

The popular robotics simulator Gazebo [15] can utilize several different physics engines to simulate multi-rigid-body contact dynamics; Bullet [11] is a common choice. This engine models hard contact dynamics with a linear complementarity problem (LCP) that is solved at each time step [16]. Similar engines like DART [8] and Drake [6] also employ LCP models. In order to fit the LCP problem formulation, a system’s dynamics are discretized using first-order Euler integration. High sample rates are then often required. Gradients through these physics engines can always be computed using a finite-difference scheme, although this may be computationally expensive. Stochastic schemes, like gradient bundles [17], potentially provide smoothed gradients and require less samples, but are still computationally expensive. Automatic differentiation tools have also been utilized to compute gradients [11]. However, because of the discontinuous nature of contact dynamics, this approach will sometimes return sub-gradients, which do not provide useful information through contact events. Heuristics have been proposed to enumerate contact modes in order to select informative sub-gradients [8]. However, this approach scales poorly with the number of mode switches.

Engines designed for hardware acceleration (e.g., GPUs), including Brax [7] and PhysX [18], utilize simplified dynamics and contact models to enable parallel computation that results in high sample rates. However, the simulation results are typically low-fidelity.

3 Technical Background

This section provides important background information on complementarity-based contact models and implicit differentiation.

3.1 Complementarity-Based Contact Models

Impacts and friction can be modeled through constraints on the system’s configuration and the applied contact impulses. The set of constraints,

$$\phi(z) \geq 0, \gamma \geq 0, \gamma \circ \phi(z) = 0, \quad (1)$$

where $z \in \mathbf{Z}$ is the robot configuration, $\phi : \mathbf{Z} \rightarrow \mathbf{R}^P$ is a signed-distance function indicating the distance to a contact surface for P contact points, $\gamma \in \mathbf{R}^P$ are normal impulses applied to each contact point, and \circ is the Hadamard (element-wise) product, model impacts [16].

Similarly, the set of constraints,

$$v - \eta_{(2:3)} = 0, \beta_{(1)} - \mu\gamma = 0, \beta \circ \eta = 0, \quad (2)$$

$$\|\beta_{(2:3)}\|_2 \leq \beta_{(1)}, \|\eta_{(2:3)}\|_2 \leq \eta_{(1)}, \quad (3)$$

with tangential velocity of a point $v \in \mathbf{R}^2$, $\beta, \eta \in \mathbf{R}^3$, and friction coefficient $\mu \in \mathbf{R}_+$ are derived from the maximum dissipation principle and model Coulomb friction [19]. The friction impulses applied to the system are $\beta_{(2:3)}$.

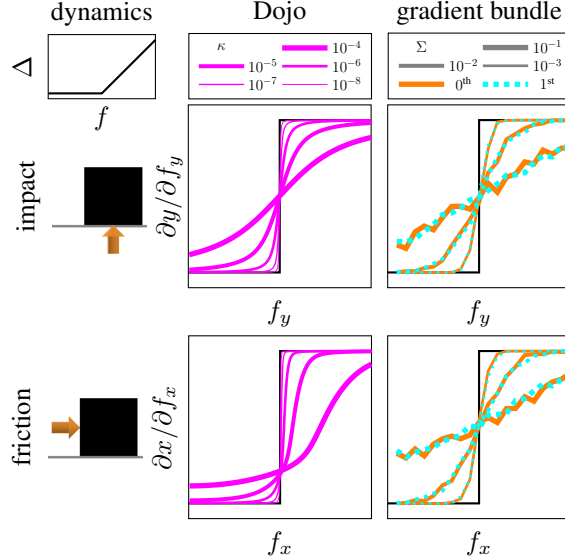


Figure 2: Gradient comparison between subgradients (black), gradient bundles [17] (orange, blue) and Dojo’s analytic gradients (magenta). The dynamics for a box in the XY plane that is resting on a flat surface and displaced an amount Δ by a force f (top left). Gradient bundles (right column) are computed using 500 samples with varying covariances Σ . Dojo’s gradients (middle column) are computed for different values of central-path parameter κ . Compared to Dojo, the gradient bundle method produces noisy derivatives that are many times more expensive to compute.

To simulate a system, a nonlinear complementarity problem (NCP), comprising the impact and friction constraints (1-3) and discrete-time system dynamics, is solved to find the contact impulses and next configuration. Often, the impact and friction constraints are locally linearized to form an LCP [16], which can be solved using a pivoting algorithm [20]. A comparison of friction-cones is provided in Appendix A.

3.2 Implicit-Function Theorem

An implicit function, $r : \mathbf{R}^{n_w} \times \mathbf{R}^{n_\theta} \rightarrow \mathbf{R}^{n_w}$, is defined as $r(w^*; \theta) = 0$ for solution $w^* \in \mathbf{R}^{n_w}$ and problem data $\theta \in \mathbf{R}^{n_\theta}$. At a solution point, the sensitivities of the solution with respect to the problem data, i.e., $\partial w^* / \partial \theta$, can be computed [21]. First, we approximate the function at the solution to first order:

$$\frac{\partial r}{\partial w} \delta w + \frac{\partial r}{\partial \theta} \delta \theta = 0, \quad (4)$$

and then solve for the relationship:

$$\frac{\partial w^*}{\partial \theta} = -\left(\frac{\partial r}{\partial w}\right)^{-1} \frac{\partial r}{\partial \theta}. \quad (5)$$

Newton’s method is typically employed to find solutions. When the method succeeds, the sensitivity (5) can be computed and the factorization of $\partial r / \partial w$ used to find the solution is reused to efficiently compute sensitivities at very low computational cost, using only back-substitution. Additionally, each element of the sensitivity can be computed in parallel.

4 Dojo

We now present Dojo’s contact dynamics model and custom interior-point solver. An open-source implementation is provided. Additional details are found with the implementation and in the Appendices.

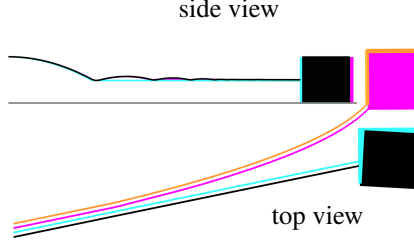


Figure 3: Velocity drift resulting from friction-cone approximation. Comparison between a box sliding with approximate cones having four vertices implemented in MuJoCo (magenta) and Dojo (orange) versus MuJoCo’s (black) and Dojo’s (blue) nonlinear friction cones. Dojo’s nonlinear friction cone gives the physically correct straight line motion, while linear friction-cone approximations lead to lateral drift. MuJoCo’s nonlinear friction cone exhibits a minor rotational drift.

4.1 Contact Dynamics Model

Dojo utilizes a maximal-coordinates state representation [22]. Each body has linear:

$$m(p_+ - 2p + p_-)/h - hmg - A(p)^T j - hf = 0, \quad (6)$$

and rotational:

$$\sqrt{1 - \psi_+^T \psi_+} J \psi_+ + \psi_+ \times J \psi_+ - \sqrt{1 - \psi^T \psi} J \psi + \psi \times J \psi - B(q)^T j - h^2 \tau / 2 = 0, \quad (7)$$

dynamics specified by mass $m \in \mathbf{R}_{++}$, inertia $J \in \mathbf{S}_{++}^3$, gravity $g \in \mathbf{R}^3$, and time step $h \in \mathbf{R}_{++}$. Equations (6, 7) are essentially second-order centered-finite-difference approximations of Newton’s second law and Euler’s equation for the rotational dynamics where $q_+ = q \cdot (\sqrt{1 - \psi_+^T \psi_+}, \psi_+)$ is recovered from a three-parameter representation $\psi \in \mathbf{R}^3$ [23], respectively. Joint impulses $j \in \mathbf{J}$ have linear $A : \mathbf{R}^3 \rightarrow \mathbf{R}^{\dim(\mathbf{J}) \times 3}$ and rotational $B : \mathbf{H} \rightarrow \mathbf{R}^{\dim(\mathbf{J}) \times 3}$ mappings into the dynamics, where \mathbf{H} is the space of unit quaternions. The configuration of a body $z^{(i)} = (p^{(i)}, q^{(i)}) \in \mathbf{R}^3 \times \mathbf{H}$ comprises a position and orientation represented as a quaternion. Forces and torques $f, \tau \in \mathbf{R}^3$ can be applied to the bodies. These integrators automatically conserve momentum and energy [24]. Additional details are provided in Appendix B.

Systems comprising N bodies and P contact points are simulated using a time-stepping scheme that solves the feasibility problem,

$$\begin{aligned} \text{find} \quad & z_+, j, \gamma, s, \beta^{(1:P)}, \eta^{(1:P)} \\ \text{s.t.} \quad & F(z_-, z, z_+, j, \lambda, u) = 0, \\ & s - \phi(z_+) = 0, \\ & \gamma \circ s = \kappa \mathbf{1}, \\ & \beta^{(i)} \circ \eta^{(i)} = \kappa \mathbf{e}, \quad i = 1, \dots, P, \\ & v^{(i)}(z, z_+) - \eta^{(i)}_{(2:3)} = 0, \quad i = 1, \dots, P, \\ & \beta^{(i)}_{(1)} - \mu^{(i)} \gamma^{(i)} = 0, \quad i = 1, \dots, P, \\ & \gamma^{(i)}, s^{(i)} \geq 0, \|\beta^{(i)}_{(2:3)}\|_2 \leq \beta^{(i)}_{(1)}, \|\eta^{(i)}_{(2:3)}\|_2 \leq \eta^{(i)}_{(1)}, \quad i = 1, \dots, P, \end{aligned} \quad (8)$$

at each time step with slack variables $s \in \mathbf{R}^P$, actions $u = (f^{(1)}, \tau^{(1)}, \dots, f^{(N)}, \tau^{(N)}) \in \mathbf{U}$, contact impulses $\lambda = (\beta^{(1)}_{(2:3)}, \gamma^{(1)}, \dots, \beta^{(P)}_{(2:3)}, \gamma^{(P)}) \in \Lambda$. The system’s smooth dynamics $F : \mathbf{Z} \times \mathbf{Z} \times \mathbf{Z} \times \mathbf{J} \times \Lambda \times \mathbf{U} \rightarrow \mathbf{R}^{6N}$ comprise linear and rotational dynamics (6-7) for each body [22]. The central-path parameter $\kappa \in \mathbf{R}_+$ and target \mathbf{e} [25] are utilized by the interior-point solver in the following section.

Solving the NCP finds a maximal-coordinates state representation. In many applications it is desirable to utilize a minimial-coordinates representation (e.g., direct trajectory optimization where algorithm complexity scales with the state dimension). Dojo includes functionality to analytically convert between representations, as well as formulate and apply the appropriate chain rule in order to differentiate through a representation transformation.

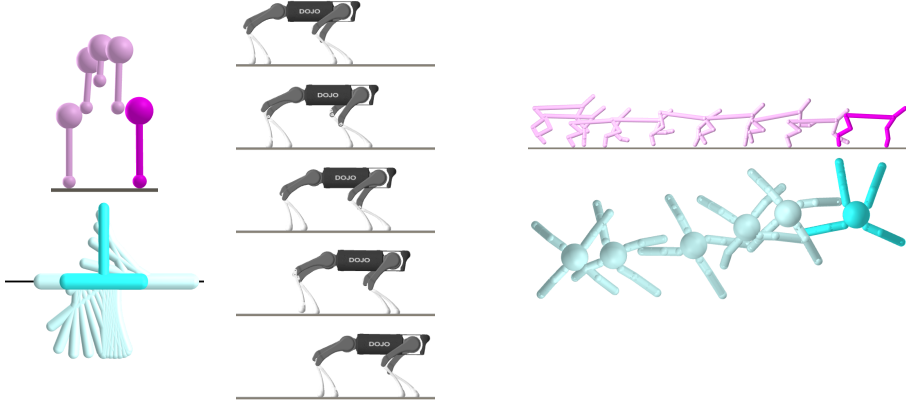


Figure 4: Motion plans for hopper (top left), cart-pole (bottom left), and quadruped (middle) generated using trajectory optimization. Rollouts for half-cheetah (top right) and ant (bottom right) generated using policies trained with reinforcement learning.

4.2 Primal-Dual Interior-Point Solver

To efficiently and reliably satisfy (8), we developed a custom primal-dual interior-point solver for NCPs with cone constraints and quaternions. The algorithm is largely based upon Mehrotra’s predictor-corrector algorithm [26, 27], while implementing non-Euclidean optimization techniques to handle quaternions [28] and borrowing features from CVXOPT [25] to handle cones.

The solver aims to satisfy instantiations of the following problem:

$$\begin{aligned}
 & \text{find} && a, b, c \\
 & \text{subject to} && E(a, b, c; \theta) = 0, \\
 & && b \circ c = \kappa \mathbf{e}, \\
 & && b, c \in \mathcal{K},
 \end{aligned} \tag{9}$$

with decision variables $a \in \mathbf{R}^{n_a}$ and $b, c \in \mathbf{R}^{n_K}$, equality-constraint set $E : \mathbf{R}^{n_a} \times \mathbf{R}^{n_K} \times \mathbf{R}^{n_K} \times \mathbf{R}^{n_\theta} \rightarrow \mathbf{R}^{n_a+n_K}$, problem data $\theta \in \mathbf{R}^{n_\theta}$; and where \mathcal{K} is the Cartesian product of positive-orthant and second-order cones [29]. We note that LCPs are a special-case of (9).

Interior-point methods aim to satisfy a sequence of relaxed problems with $\kappa > 0$ and $\kappa \rightarrow 0$ in order to reliably converge to a solution of the original problem (i.e., $\kappa = 0$). This continuation approach helps avoid premature ill-conditioning and is the basis for numerous convex and non-convex interior-point solvers [27].

For an instance of problem (9), the algorithm is provided problem data and an initial point, which is projected to ensure that the cone variables are initially feasible with some margin. Next, an affine search direction (i.e., predictor) is computed that aims for zero complementarity violation. Using this direction, a cone line search is performed followed by a centering step that computes a target relaxation for the computation of the corrector search direction. A second cone line search is then performed for this new search direction. A subsequent line search is performed until either the constraint or complementarity violation is reduced. The current point is then updated, a new affine search direction is computed, and the procedure repeats until the violations satisfy the solver tolerances. Additional details and an algorithm are provided in Appendix C.

Interior-point methods solve non-smooth problems by optimizing a sequence of smooth barrier subproblems, where the degree of smoothing is parameterized by the central-path parameter κ . In the contact setting, we employ this same technique to return gradients that are informative through contact events. Intermediate solutions, $w^*(\theta, \kappa > 0)$, are differentiated using the implicit-function theorem (5) to compute smooth *implicit gradients*. In practice, we find that these gradients greatly improve the performance of gradient-based optimization methods, consistent with the long history of interior-point methods. Dojo’s gradients are compared with sub-gradients and gradient bundles in Fig. 2. A wall-clock-time comparison of these gradients and sampled gradients is provided in

Table 3: Trajectory-optimization results. Comparison of final cost value, goal constraint violation, and total number of iterations for a collection of systems with maximal (max) and minimal (min) representations, optimized with iterative LQR [30] using Dojo with implicit gradients or MuJoCo (M) with finite-difference gradients. Final results are comparable across all systems, but importantly, Dojo enforces hard contact in contrast to MuJoCo’s soft contact. Further, the implicit gradients are significantly less expensive to compute.

system	cost	violation	iterations
cart-pole (max)	30.2	2e-3	100
cart-pole (min)	35.5	3e-5	100
cart-pole (M)	37.0	5e-4	80
box right (max)	14.5	3e-3	30
box right (M)	13.5	3e-3	95
box up (max)	14.5	3e-3	106
box up (M)	failure	1.0	-
hopper (max)	10.2	4e-3	57
hopper (min)	8.9	1e-3	96
hopper (M)	26.7	2e-3	66
quadruped (min)	2e-2	3e-4	20

Appendix E, demonstrating that implicit gradients are more than an order of magnitude faster to compute.

The problem data for each simulation step include: the previous and current configurations, action, and additional terms like the time step, friction coefficients, and parameters of each body.

4.3 Open-Source Implementation

An open-source implementation, `Dojo.jl`, written in Julia, is available and a Python interface, `dojopy`, is also included. These tools, and the experiment, are available at: <https://github.com/dojo-sim>.

5 Experimental Results

5.1 Simulation

The simulation accuracy of Dojo and MuJoCo is compared in a number of illustrative scenarios.

The Atlas humanoid is simulated dropping on to a flat surface (Fig. 1). The system comprises 31 bodies, resulting in 403 maximal-coordinates states, and has 36 actuated degrees-of-freedom. Each foot has four contact points. The current implementation of Dojo simulates this system in real time at 65 Hz. A comparison with MuJoCo is performed measuring penetration violations with the floor for different simulation rates (Table 2)

The effect of friction-cone approximation is demonstrated by simulating a box that is initialized with lateral velocity before impacting and sliding along a flat surface. For a pyramidal approximation, in the probable scenario where its vertices are not aligned with the direction of motion, velocity drift occurs for a linearized cone implemented in Dojo and MuJoCo (Fig. 3). The complementarity problem with P contact points requires $2P(1+2d)$ decision variables for contact and a corresponding number of constraints, where d is the degree of parameterization (e.g., double parameterization: $d = 2$). While it is possible to reduce such artifacts by increasing the number of vertices in the approximation of the second-order cone, this increases the computational complexity. Such approximation is unnecessary in Dojo as we handle the exact nonlinear cone constraint efficiently and reliably with optimization tools from cone programming; the result is accurate sliding.

5.2 Trajectory Optimization

Iterative LQR [31] utilizes implicit gradients from Dojo to perform trajectory optimization on four systems: cart-pole, planar box, hopper, and quadruped. Additional details are found in Appendix G.

Table 4: Reinforcement-learning results for policy optimization. Comparison of total reward, number of simulation-step and gradient evaluations for a collection of policies trained with Augmented Random Search (ARS) [32] and Augmented Gradient Search (AGS). The results are averaged over the best 3 out of 5 runs with different random seeds. Optimizing with gradients reaches similar performance levels while being 5 to 10 times more sample efficient.

system	reward	simulation	gradient
half-cheetah (ARS)	46 \pm 24	3e+4	0
ant (ARS)	64 \pm 15	2e+5	0
half-cheetah (AGS)	44 \pm 24	5e+3	5e+3
ant (AGS)	54 \pm 28	2e+4	2e+4

A comparison is performed with MuJoCo’s finite-difference gradients. The results are visualized in Fig. 4 and summarized in Table 3.

Overall, we find that final results from both engines are similar. However, importantly, MuJoCo is enforcing soft contact whereas Dojo simulates hard contact. Further, for systems with contact, MuJoCo requires a time step $h = 0.01$ for successful optimization, whereas Dojo succeeds with $h = 0.05$. Additionally, finite-difference gradients are significantly more expensive to compute than Dojo’s implicit gradients.

5.3 Reinforcement Learning

Gym-like environments [13, 33]: ant and half-cheetah are implemented in Dojo and we train static linear policies for locomotion. Additional details are found in Appendix H. As a baseline, we employ Augmented Random Search (ARS) [32], a gradient-free approach coupling random search with a number of simple heuristics. For comparison, we train the same policies using augmented gradient search (AGS) which replaces the stochastic-gradient estimation of ARS with the Dojo’s implicit gradients. Policy rollouts are visualized in Fig. 3 and results are summarized in Table 4.

First, we are able to successfully train policies using this simple learning algorithm in Dojo’s hard contact environments. Second, MuJoCo requires smaller $h = 0.01$ time steps for stable simulation, whereas Dojo is stable with $h = 0.05$. This 5 times decrease in rollout length can help alleviate the common vanishing/exploding gradient problem and significantly reduces the overall compute required for training. Third, by utilizing implicit gradients it is possible to train comparable policies in Dojo with 5 to 10 times less samples compared to the gradient-free method.

5.4 System Identification

System identification is performed on an existing real-world dataset of trajectories collected by throwing a box on a table with different initial conditions [14]. We learn a set of parameters $\theta = (\mu, p^{(1)}, \dots, p^{(8)})$ that include the friction coefficient μ , and 3-dimensional vectors $p^{(i)}$ that represent the position of vertex i of the box with respect to its center of mass.

Each trajectory is decomposed into $T - 2$ triplets of consecutive configurations: $Z = (z_-, z, z_+)$, where T is the number of time steps in the trajectory. Using the initial conditions z_- , z from a tuple, and an estimate of the system’s parameters θ , Dojo performs one-step simulation to predict the next state, \hat{z}_+ . Implicit gradients are utilized by a Gauss Newton method to perform gradient-based learning. Additional details are found in Appendix I.

6 Limitations

The computation cost of Dojo per simulation step is greater than many existing engines. This cost enables superior simulation accuracy at the cost of greater wall-clock time and is a trade-off that must be considered by the user for a particular application. Because Dojo solves a NCP (i.e, non-convex problem) at each time step the engine provides no guarantees of converging to a solution. In practice, we do not find this to be a problem, but for time- or safety-critical applications this should be a consideration. Finally, our preliminary hardware experiments have demonstrated that simulation

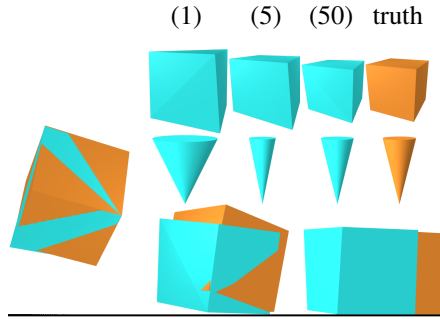


Figure 5: System identification. Top right: Learning box geometry and friction cone to less than 5% error. Bottom: Simulated trajectory of the box using the learned properties (blue) compared to ground truth (orange).

in Dojo transfers to quadrupedal hardware using model-predictive control [34]. However, it remains to be seen how well the transfer works for manipulation tasks and, more generally, in comparison to existing engines.

7 Conclusion

Dojo is designed from physics- and optimization-first principles to enable better optimization for motion planning, control, reinforcement learning, and system identification. The engine makes several advancements over previous state-of-the-art engines for robotics: First, the variational integrator enables stable simulation at low sample rates. We demonstrate a 5 times decrease in physics-engine evaluations for planning and policy optimization, leading to a substantial reduction in algorithm complexity. Second, the contact model includes a higher fidelity friction model that eliminates artifacts like creep, particularly for sliding, and hard contact for impact is achieved to machine precision. This should enable superior sim-to-real transfer for both locomotion and manipulation applications. The underlying interior-point solver, developed specifically for solving NCPs, is numerically robust and requires practically no hyperparameter tuning for good performance across numerous systems, and handles cone and quaternion variables. Third, the engine efficiently returns implicit gradients that are smooth and analytical, providing useful information through contact events while enabling a 5 to 10 times improvement in sample complexity for policy optimization. In addition to building and providing an open-source tool, the physics and optimization algorithms presented can improve many existing engines.

After training, the learned parameters are within 5% of the geometry and best-fit friction coefficient for the box from the dataset. We perform real-to-sim and simulate the system in Dojo, comparing it to the dataset trajectories. Results are visualized in Fig. 5.

A number of future improvements to Dojo are planned. First, Dojo currently implements simple collision detection (e.g., sphere-halfspace, sphere-sphere, sphere-box). Natural extensions include support for general curved surfaces and complex body geometries. Another improvement is adaptive time stepping. Similar to advanced numerical integrators for stiff systems, Dojo should take large time steps when possible and adaptively modify the time step in cases of numerical difficulties or physical inaccuracies. Finally, greater exploitation of algorithmic parallelism in Dojo would enable faster simulation and optimization.

Acknowledgements

The authors would like to thank Jan Brüdigam for his open-source library `ConstrainedDynamics.jl`, which served as a foundation for Dojo’s maximal-coordinates state representation, as well as early technical discussions and support; and Suvansh Sanjeev for assistance with the Python interface. Toyota Research Institute provided funds to support this work.

References

- [1] O. M. Andrychowicz, B. Baker, M. Chociej, R. Jozefowicz, B. McGrew, J. Pachocki, A. Petron, M. Plappert, G. Powell, A. Ray, et al. Learning dexterous in-hand manipulation. *The International Journal of Robotics Research*, 39(1):3–20, 2020.
- [2] I. Akkaya, M. Andrychowicz, M. Chociej, M. Litwin, B. McGrew, A. Petron, A. Paino, M. Plappert, G. Powell, R. Ribas, et al. Solving Rubik’s cube with a robot hand. *arXiv preprint arXiv:1910.07113*, 2019.
- [3] J. Lee, J. Hwangbo, L. Wellhausen, V. Koltun, and M. Hutter. Learning quadrupedal locomotion over challenging terrain. *Science Robotics*, 5(47), 2020.
- [4] A. Kumar, Z. Fu, D. Pathak, and J. Malik. RMA: Rapid motor adaptation for legged robots. *arXiv preprint arXiv:2107.04034*, 2021.
- [5] S. Levine, P. Pastor, A. Krizhevsky, J. Ibarz, and D. Quillen. Learning hand-eye coordination for robotic grasping with deep learning and large-scale data collection. *The International journal of robotics research*, 37(4-5):421–436, 2018.
- [6] R. Tedrake and the Drake Development Team. Drake: Model-based design and verification for robotics, 2019. URL <https://drake.mit.edu>.
- [7] C. D. Freeman, E. Frey, A. Raichuk, S. Girgin, I. Mordatch, and O. Bachem. Brax-A differentiable physics engine for large scale rigid body simulation. *arXiv preprint arXiv:2106.13281*, 2021.
- [8] K. Werling, D. Omens, J. Lee, I. Exarchos, and C. K. Liu. Fast and feature-complete differentiable physics for articulated rigid bodies with contact. *arXiv preprint arXiv:2103.16021*, 2021.
- [9] M. Geilinger, D. Hahn, J. Zehnder, M. Bächer, B. Thomaszewski, and S. Coros. ADD: Analytically differentiable dynamics for multi-body systems with frictional contact. *ACM Transactions on Graphics (TOG)*, 39(6):1–15, 2020.
- [10] Y. Hu, L. Anderson, T.-M. Li, Q. Sun, N. Carr, J. Ragan-Kelley, and F. Durand. DiffTaichi: Differentiable programming for physical simulation. *ICLR*, 2020.
- [11] E. Heiden, D. Millard, E. Coumans, Y. Sheng, and G. S. Sukhatme. NeuralSim: Augmenting differentiable simulators with neural networks. In *Proceedings of the IEEE International Conference on Robotics and Automation (ICRA)*, 2021. URL <https://github.com/google-research/tiny-differentiable-simulator>.
- [12] E. Todorov, T. Erez, and Y. Tassa. MuJoCo: A physics engine for model-based control. In *2012 IEEE/RSJ International Conference on Intelligent Robots and Systems*, pages 5026–5033. IEEE, 2012.
- [13] G. Brockman, V. Cheung, L. Pettersson, J. Schneider, J. Schulman, J. Tang, and W. Zaremba. OpenAI Gym, 2016.
- [14] S. Pfrommer, M. Halm, and M. Posa. ContactNets: Learning discontinuous contact dynamics with smooth, implicit representations. *arXiv preprint arXiv:2009.11193*, 2020.
- [15] N. Koenig and A. Howard. Design and use paradigms for Gazebo, an open-source multi-robot simulator. In *2004 IEEE/RSJ International Conference on Intelligent Robots and Systems (IROS)(IEEE Cat. No. 04CH37566)*, volume 3, pages 2149–2154. IEEE, 2004.
- [16] D. E. Stewart and J. C. Trinkle. An implicit time-stepping scheme for rigid body dynamics with inelastic collisions and coulomb friction. *International Journal for Numerical Methods in Engineering*, 39(15):2673–2691, 1996.
- [17] H. J. Terry Suh, T. Pang, and R. Tedrake. Bundled gradients through contact via randomized smoothing. *arXiv preprint arXiv:2109.05143*, 2021.
- [18] Physx physics engine, 2022. URL <https://developer.nvidia.com/physx-sdk>.

[19] J. J. Moreau. On unilateral constraints, friction and plasticity. In *New Variational Techniques in Mathematical Physics*, pages 171–322. Springer, 2011.

[20] R. W. Cottle, J.-S. Pang, and R. E. Stone. *The linear complementarity problem*. SIAM, 2009.

[21] U. Dini. *Lezioni di analisi infinitesimale*, volume 1. Fratelli Nistri, 1907.

[22] J. Brüdigam and Z. Manchester. Linear-time variational integrators in maximal coordinates. *arXiv preprint arXiv:2002.11245*, 2020.

[23] Z. R. Manchester and M. A. Peck. Quaternion variational integrators for spacecraft dynamics. *Journal of Guidance, Control, and Dynamics*, 39(1):69–76, 2016.

[24] J. E. Marsden and M. West. Discrete mechanics and variational integrators. *Acta Numerica*, 10:357–514, 2001.

[25] L. Vandenberghe. The CVXOPT linear and quadratic cone program solvers. *Online: <http://cvxopt.org/documentation/coneprog.pdf>*, 2010.

[26] S. Mehrotra. On the implementation of a primal-dual interior point method. *SIAM Journal on Optimization*, 2(4):575–601, 1992.

[27] J. Nocedal and S. J. Wright. *Numerical Optimization*. Springer, second edition, 2006.

[28] B. E. Jackson, K. Tracy, and Z. Manchester. Planning with attitude. *IEEE Robotics and Automation Letters*, 6(3):5658–5664, 2021.

[29] S. Boyd and L. Vandenberghe. *Convex optimization*. Cambridge University Press, 2004.

[30] W. Li and E. Todorov. Iterative linear quadratic regulator design for nonlinear biological movement systems. In *ICINCO (1)*, pages 222–229. Citeseer, 2004.

[31] T. A. Howell, S. Le Cleac'h, S. Singh, P. Florence, Z. Manchester, and V. Sindhwan. Trajectory optimization with optimization-based dynamics. *arXiv preprint arXiv:2109.04928*, 2021.

[32] H. Mania, A. Guy, and B. Recht. Simple random search of static linear policies is competitive for reinforcement learning. In *Advances in Neural Information Processing Systems*, pages 1800–1809, 2018.

[33] Y. Duan, X. Chen, R. Houthooft, J. Schulman, and P. Abbeel. Benchmarking deep reinforcement learning for continuous control. In *International Conference on Machine Learning*, pages 1329–1338. PMLR, 2016.

[34] S. Le Cleac'h, T. A. Howell, M. Schwager, and Z. Manchester. Fast contact-implicit model-predictive control. *arXiv preprint arXiv:2107.05616*, 2021.

[35] T. Erez, Y. Tassa, and E. Todorov. Simulation tools for model-based robotics: Comparison of Bullet, Havok, MuJoCo, ODE and PhysX. In *2015 IEEE International Conference on Robotics and Automation (ICRA)*, pages 4397–4404. IEEE, 2015.

[36] H. Sharma, M. Patil, and C. Woolsey. Energy-preserving variational integrators for forced lagrangian systems. *Communications in Nonlinear Science and Numerical Simulation*, 64:159–177, 2018.

[37] R. Tedrake. Underactuated robotics: Algorithms for walking, running, swimming, flying, and manipulation (course notes for MIT 6.832). *Downloaded in Fall, 2021*.

[38] M. H. Raibert, H. B. Brown Jr., M. Chepponis, J. Koechling, J. K. Hodgins, D. Dustman, W. K. Brennan, D. S. Barrett, C. M. Thompson, J. D. Hebert, W. Lee, and B. Lance. Dynamically stable legged locomotion. Technical report, Massachusetts Institute of Technology Cambridge Artificial Intelligence Lab, 1989.

Appendix A: Friction Cone Comparison

The classic LCP formulation for contact dynamics results in a linearized friction cone. Our NCP formulation utilizes an unmodified second-order cone. These cones are visualized in Fig. 6.

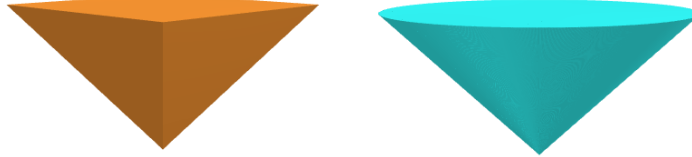


Figure 6: Friction-cone comparison. Linearized double-parameterized (left) and nonlinear second-order (right) cones.

Appendix B: Maximal-Coordinates State Representation

Most robotics physics engines utilize minimal- or joint-coordinates representations for dynamics because of the small number of states and convenience of implementation. This results in small, but dense systems of linear equations. In contrast, maximal-coordinates explicitly represent the position, orientation, and velocities of each body in a multi-rigid-body system. This produces large, sparse systems of linear equations that can be efficiently optimized, including in the contact setting, and provides more information about a system at each simulation step. We provide an overview, largely based on prior work [22], of this representation.

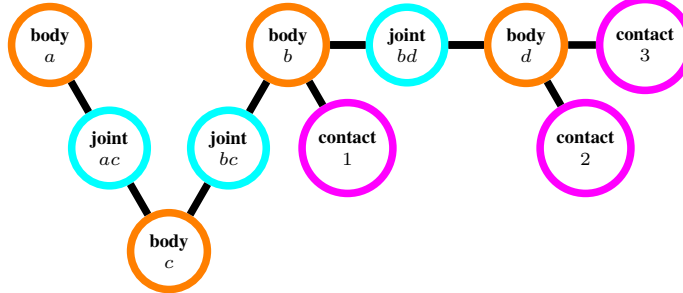


Figure 7: Graph structure for maximal-coordinates system with 4 bodies, 3 joints, and 3 points of contact.

A single rigid body is defined by its mass and inertia, and has a configuration, $x = (p, q) \in \mathbf{X} = \mathbf{R}^3 \times \mathbf{H}$, comprising a position p and unit quaternion q , where \mathbf{H} is the space of four-dimensional unit quaternions. We define the implicit discrete-time dynamics $F : \mathbf{X} \times \mathbf{X} \times \mathbf{X} \rightarrow \mathbf{R}^6$ as:

$$F(x_-, x, x_+) = 0, \quad (10)$$

where we indicate the previous and next time steps with minus (−) and plus (+) subscripts, respectively, and the current time step without decoration. A variational integrator is employed that has desirable energy and momentum conservation properties [24]. Linear and angular velocities are handled implicitly via finite-difference approximations.

For a multi-rigid-body system with bodies a and b connected via a joint—common types include: revolute, prismatic, and spherical—we introduce a constraint, $k : \mathbf{X} \times \mathbf{X} \rightarrow \mathbf{R}^l$, that couples the two bodies:

$$k^{ab}(x_+^a, x_+^b) = 0. \quad (11)$$

An impulse, $j \in \mathbf{R}^l$, where l is equal to the six degrees-of-freedom of an unconstrained body minus the joint's number of degrees-of-freedom, acts on both bodies to satisfy the constraint. The implicit integrator for the multi-rigid-body system has the form,

$$\begin{bmatrix} F^a(x_-^a, x^a, x_+^a) + K^a(x^a, x^b)^T j^{ab} \\ F^b(x_-^b, x^b, x_+^b) + K^b(x^a, x^b)^T j^{ab} \\ k^{ab}(x_+^a, x_+^b) \end{bmatrix} = 0, \quad (12)$$

where $K : \mathbf{X} \times \mathbf{X} \rightarrow \mathbf{R}^{l \times 6}$ is a mapping from the joint to the maximal-coordinates space and is related to the Jacobian of the joint constraint.

We can generalize (12) to include additional bodies and joints. For a system with N bodies and M joints we define a maximal-coordinates configuration $z = (x^{(1)}, \dots, x^{(N)}) \in \mathbf{Z}$ and joint impulse $j = (j^{(1)}, \dots, j^{(M)}) \in \mathbf{J}$. We define the implicit discrete-time dynamics of the maximal-coordinates system as:

$$F(z_-, z, z_+, j) = 0, \quad (13)$$

where $F : \mathbf{Z} \times \mathbf{Z} \times \mathbf{Z} \times \mathbf{J} \rightarrow \mathbf{R}^{6N}$. In order to simulate the system we find z_+ and j that satisfy (13) for a provided z_- and z using Newton's method.

By exploiting the mechanism's structure, we can efficiently perform root finding on (13) (see [22] for additional details). This structure is manifest as a graph of the mechanism, where each body and joint is considered a node, and joints have edges connecting bodies (Fig. 7). Because the mechanism structure is known *a priori*, a permutation matrix can be precomputed and used to perform efficient sparse linear algebra during simulation. For instance, in the case where the joint constraints form a system without loops, the resulting sparse system can be solved in linear time with respect to the number of links.

An equivalent version of the rotation dynamics,

$$VL(q)^T \left(TR(q_+)^T V^T JVL(q)^T q_+ + L(q_-)^T V^T JVL(q_-)^T q \right) / h - B(q)^T j - h\tau = 0, \quad (14)$$

is expressed with quaternions. The matrix notation we use for quaternion operations: L, R, V, T , are defined in prior work [22] and are provided in Appendix D.

Appendix C: Solver Algorithms

Residual and Jacobians. The interior-point solver aims to find a fixed point for the residual:

$$r(w; \theta, \kappa) = \begin{bmatrix} E(w; \theta) \\ b^{(1)} \circ c^{(1)} - \kappa \mathbf{1} \\ \vdots \\ b^{(n\kappa)} \circ c^{(n\kappa)} - \kappa \mathbf{e} \end{bmatrix}, \quad (15)$$

while respecting the cone constraints. The Jacobian of this residual with respect to the decision variables,

$$R(w; \theta) = \partial r(w; \theta, \cdot) / \partial w, \quad (16)$$

is used to compute a search direction. For convenience, we denote $w = (a, b, c)$. After a solution $w^*(\theta, \kappa)$ is found, the Jacobian of the residual with respect to the problem data,

$$D(w; \theta) = \partial r(w; \theta, \cdot) / \partial \theta, \quad (17)$$

is used to compute the sensitivity of the solution. These Jacobians are not explicitly dependent on the central-path parameter.

The non-Euclidean properties of quaternion variables are handled with modifications to these Jacobians (16) and (17) by right multiplying each with a matrix H containing attitude Jacobians [28] corresponding to the quaternions in x and θ , respectively:

$$\bar{R}(w; \theta) = R(w; \theta)H_R(w), \quad (18)$$

$$\bar{D}(w; \theta) = D(w; \theta)H_D(\theta). \quad (19)$$

Euclidean variables have corresponding identity blocks. This modification accounts for the implicit unit-norm constraint on each quaternion variable and improves the convergence behaviour of the solver.

Cones. The generalized inequality, cone-product operator, and the target for the n -dimensional positive orthant are:

$$\mathbf{R}_{++}^n = \{a \in \mathbf{R}^n \mid a_{(i)} > 0, i = 1, \dots, n\}, \quad (20)$$

$$a \circ b = (a_{(1)}b_{(1)}, \dots, a_{(n)}b_{(n)}), \quad (21)$$

$$\mathbf{e} = \mathbf{1}. \quad (22)$$

For the second-order cone:

$$\mathcal{Q}^n = \{(a_{(1)}, a_{(2:n)}) \in \mathbf{R} \times \mathbf{R}^{n-1} \mid \|a_{(2:n)}\|_2 \leq a_{(1)}\}, \quad (23)$$

$$a \circ b = (a^T b, a_{(1)} b_{(2:n)} + a_{(1)} b_{(2:n)}), \quad (24)$$

$$\mathbf{e} = (1, 0, \dots, 0). \quad (25)$$

The solver utilizes the Cartesian product,

$$\mathcal{K} = \mathbf{R}_+^n \times \mathcal{Q}_1^{l_1} \times \dots \times \mathcal{Q}_j^{l_j}, \quad (26)$$

of the n -dimensional positive orthant and j second-order cones, each of dimension l_i .

Analytical line search for cones. To ensure the cone variables strictly satisfy their constraints, a cone line search is performed for a candidate search direction. For the update:

$$y \leftarrow y + \alpha \Delta, \quad (27)$$

with step size α and search direction Δ , the solver finds the largest $\alpha \in [0, 1]$ such that $y + \alpha \Delta \in \mathcal{K}$. The step-size is computed analytically for the positive orthant:

$$\alpha = \min \left(1, \max_{k|\Delta_{(k)} < 0} \left\{ -\frac{y_{(k)}}{\Delta_{(k)}} \right\} \right), \quad (28)$$

and second-order cone:

$$\nu = y_{(1)}^2 - y_{(2:k)}^T y_{(2:k)}, \quad (29)$$

$$\zeta = y_{(1)} \Delta_{(1)} - y_{(2:k)}^T \Delta_{(2:k)}, \quad (30)$$

$$\rho_{(1)} = \frac{\zeta}{\nu}, \quad (31)$$

$$\rho_{(2:k)} = \frac{\Delta_{(2:k)}}{\sqrt{\nu}} - \frac{\zeta/\sqrt{\nu} + \Delta_{(1)}}{y_{(1)}/\sqrt{\nu} + 1} \frac{y_{(2:k)}}{\nu}, \quad (32)$$

$$\alpha = \begin{cases} \min \left(1, \frac{1}{\|\rho_{(2:k)}\|_2 - \rho_{(1)}} \right), & \|\rho_{(2:k)}\|_2 > \rho_{(1)}, \\ 1, & \text{otherwise.} \end{cases} \quad (33)$$

The line search over all individual cones is summarized in Algorithm 1.

Algorithm 1 Analytical Line Search For Cones

```

1: procedure CONELINESEARCH( $w, \Delta, \tau^{\text{ort}}, \tau^{\text{soc}}$ )
2:    $\alpha_y^{\text{ort}} \leftarrow \alpha(y^{(1)}, \tau^{\text{ort}} \Delta^{y^{(1)}})$   $\triangleright$  Eq. 28
3:    $\alpha_z^{\text{ort}} \leftarrow \alpha(z^{(1)}, \tau^{\text{ort}} \Delta^{z^{(1)}})$   $\triangleright$  Eq. 28
4:    $\alpha_y^{\text{soc}} \leftarrow \min_{i \in \{2, \dots, n\}} \alpha(y^{(i)}, \tau^{\text{soc}} \Delta^{y^{(i)}})$   $\triangleright$  Eq. 33
5:    $\alpha_z^{\text{soc}} \leftarrow \min_{i \in \{2, \dots, n\}} \alpha(z^{(i)}, \tau^{\text{soc}} \Delta^{z^{(i)}})$   $\triangleright$  Eq. 33
6:   Return  $\min(\alpha_y^{\text{ort}}, \alpha_z^{\text{ort}}, \alpha_y^{\text{soc}}, \alpha_z^{\text{soc}})$ 

```

Candidate update. The variables are partitioned: $a = (a^{(1)}, \dots, a^{(p)})$, where $i = 1$ are Euclidean variables and $i = 2, \dots, p$ are each quaternion variables; and $b = (b^{(1)}, \dots, b^{(n)})$, $c = (c^{(1)}, \dots, c^{(n)})$, where $j = 1$ is the positive-orthant and the remaining $j = 2, \dots, n$ are second-order cones. For a given search direction, updates for Euclidean and quaternion variables are performed. The Euclidean variables in a use a standard update:

$$a^{(1)} \leftarrow a^{(1)} + \alpha \Delta^{(1)}, \quad (34)$$

For each quaternion variable, the search direction exists in the space tangent to the unit-quaternion hypersphere and is 3-dimensional. The corresponding update for $i = 2, \dots, p$ is:

$$a^{(i)} \leftarrow L(a^{(i)}) \varphi(\alpha \Delta^{(i)}), \quad (35)$$

where $L : \mathbf{H} \rightarrow \mathbf{R}^{4 \times 4}$ is a matrix representing a left-quaternion matrix multiplication, and $\varphi : \mathbf{R}^3 \rightarrow \mathbf{H}$ is a mapping to a unit quaternion. The standard update is used for the remaining decision variables b and c .

Violation metrics. Two metrics are used to measure progress: The constraint violation,

$$r_{\text{vio}} = \|r(w; \theta)\|_\infty, \quad (36)$$

and complementarity violation,

$$\kappa_{\text{vio}} = \max_i \{ \|b^{(i)} \circ c^{(i)}\|_\infty\}. \quad (37)$$

The problem (9) is considered solved when $r_{\text{vio}} < r_{\text{tol}}$ and $\kappa_{\text{vio}} < \kappa_{\text{tol}}$.

Centering. The solver adaptively relaxes (9) by computing the centering parameters μ and σ . These values provide an estimate of the cone-constraint violation and determine the value of the central-path parameter that a correction step will aim to satisfy. These values rely on the degree of the cone [25]:

$$\mathbf{deg}(\mathcal{K}) = \sum_{i=1}^{n_{\mathcal{K}}} \mathbf{deg}(\mathcal{K}^{(i)}) = \mathbf{dim}(\mathcal{K}^{(1)}) + n_{\mathcal{K}} - 1, \quad (38)$$

the complementarity violations:

$$\mu = \frac{1}{\mathbf{deg}(\mathcal{K})} \sum_{i=1}^{n_{\mathcal{K}}} (b^{(i)})^T c^{(i)}. \quad (39)$$

and affine complementarity violations:

$$\mu^{\text{aff}} = \frac{1}{\mathbf{deg}(\mathcal{K})} \sum_{i=1}^{n_{\mathcal{K}}} (b^{(i)} + \alpha \Delta^{b^{(i)}})^T (c^{(i)} + \alpha \Delta^{c^{(i)}}), \quad (40)$$

as well as their ratio:

$$\sigma = \min \left(1, \max \left(0, \mu^{\text{aff}} / \mu \right) \right)^3, \quad (41)$$

As the algorithm makes progress, it aims to reduce these violations.

Algorithm. The interior-point algorithm used to solve (9) is summarized in Algorithm 2.

Additional tolerances $\tau \in [0.9, 1]$ are used to improve numerical reliability of the solver. The algorithm parameters include $\tau_{\text{max}}^{\text{soc}}$ to prevent the iterates from reaching the boundaries of the cones too rapidly during the solve, τ_{min} to ensure we are aiming at sufficiently large steps, and β is the decay rate of the step size α during the line search. In practice, r_{tol} and κ_{tol} are the only parameters the user might want to tune.

Finally, the algorithm outputs a solution $w^*(\theta, \kappa)$ that satisfies the solver tolerance levels and, optionally, the implicit gradients of the solution with respect to the problem parameters θ .

Algorithm 2 Primal-Dual Interior-Point Solver

```

1: procedure SOLVER( $a_0, b_0, c_0, \theta, \mathcal{K}$ )
2:   Parameters:  $\tau_{\max}^{\text{SOC}} = 0.99, \tau_{\min} = 0.95$ 
3:    $r_{\text{tol}} = 10^{-5}, \kappa_{\text{tol}} = 10^{-5}, \beta = 0.5$ 
4:   Initialize:  $a = a_0, b = b_0 \in \mathcal{K}, c = c_0 \in \mathcal{K}$ 
5:    $r_{\text{vio}}, \kappa_{\text{vio}} \leftarrow \text{VIOLATION}(w)$  ▷ (36, 37)
6:   Until  $r_{\text{vio}} < r_{\text{tol}}$  and  $\kappa_{\text{vio}} < \kappa_{\text{tol}}$  do
7:      $\Delta^{\text{aff}} \leftarrow -\bar{R}^{-1}(w; \theta)r(w; \theta, 0)$ 
8:      $\alpha^{\text{aff}} \leftarrow \text{CONESEARCH}(w, \Delta^{\text{aff}}, 1, 1)$ 
9:      $\mu, \sigma \leftarrow \text{CENTER}(b, c, \alpha^{\text{aff}}, \Delta^{\text{aff}})$  ▷ (38-41)
10:     $\kappa \leftarrow \max(\sigma\mu, \kappa_{\text{tol}}/5)$ 
11:     $\Delta \leftarrow -\bar{R}^{-1}(w; \theta)r(w; \theta, \kappa)$ 
12:     $\tau^{\text{ort}} \leftarrow \max(\tau_{\min}, 1 - \max(r_{\text{vio}}, \kappa_{\text{vio}})^2)$ 
13:     $\tau^{\text{soc}} \leftarrow \min(\tau_{\max}^{\text{SOC}}, \tau^{\text{ort}})$ 
14:     $\alpha \leftarrow \text{CONESEARCH}(w, \Delta, \tau^{\text{ort}}, \tau^{\text{soc}})$ 
15:     $c_{\text{vio}}^*, \kappa_{\text{vio}}^* \leftarrow r_{\text{vio}}, \kappa_{\text{vio}}$ 
16:     $\hat{w} \leftarrow \text{UPDATE}(w, \Delta, \alpha)$  ▷ (34, 35)
17:     $r_{\text{vio}}, \kappa_{\text{vio}} \leftarrow \text{VIOLATION}(\hat{w})$  ▷ (36, 37)
18:    Until  $r_{\text{vio}} \leq c_{\text{vio}}^*$  or  $\kappa_{\text{vio}} \leq \kappa_{\text{vio}}^*$  do
19:       $\alpha \leftarrow \beta\alpha$ 
20:       $\hat{w} \leftarrow \text{UPDATE}(w, \Delta, \alpha)$  ▷ (34, 35)
21:       $r_{\text{vio}}, \kappa_{\text{vio}} \leftarrow \text{VIOLATION}(\hat{w})$  ▷ (36, 37)
22:    end
23:     $w \leftarrow \hat{w}$ 
24:  end
25:   $\partial w^*/\partial \theta \leftarrow -\bar{R}^{-1}(w^*; \theta)\bar{D}(w^*; \theta)$  ▷ (5)
26:  Return  $w, \partial w^*/\partial \theta$ 

```

Appendix D: Quaternion Algebra

We use a set of conventions for notating standard quaternion operations adopted from [22, 28] in the rotational part of our variational integrator (7). Quaternions are written as four-dimensional vectors:

$$q = (s, v) = (s, v_1, v_2, v_3) \in \mathbf{H}, \quad (42)$$

where s and v are scalar and vector components, respectively. Dojo employs unit quaternions (i.e., $q^T q = 1$) to represent orientation, providing a mapping from the local body frame to a global inertial frame. Quaternion multiplication is performed using linear algebra (i.e., matrix-vector and matrix-matrix products). Left and right quaternion multiplication,

$$q^a \otimes q^b = \begin{bmatrix} s^a s^b - (v^a)^T v^b \\ s^a v^b + s^b v^a + v^a \times v^b \end{bmatrix} \quad (43)$$

$$= L(q^a)q^b = R(q^b)q^a, \quad (44)$$

where \times is the standard vector cross product, is represented using the matrices:

$$L(q) = \begin{bmatrix} s & -v^T \\ v & sI_3 + \text{skew}(v) \end{bmatrix} \in \mathbf{R}^{4 \times 4}, \quad (45)$$

$$R(q) = \begin{bmatrix} s & -v^T \\ v & sI_3 - \text{skew}(v) \end{bmatrix} \in \mathbf{R}^{4 \times 4}, \quad (46)$$

where,

$$\text{skew}(x) = \begin{bmatrix} 0 & -x_3 & x_2 \\ x_3 & 0 & -x_1 \\ -x_2 & x_1 & 0 \end{bmatrix}, \quad (47)$$

is defined such that,

$$\text{skew}(x)y = x \times y, \quad (48)$$

and I_3 is a 3-dimensional identity matrix. The vector component of a quaternion,

$$v = Vq, \quad (49)$$

is extracted using the matrix:

$$V = [\mathbf{0} \quad I_3] \in \mathbf{R}^{3 \times 4}, \quad (50)$$

and quaternion conjugate:

$$q^\dagger = \begin{bmatrix} s \\ -v \end{bmatrix} = Tq, \quad (51)$$

is computed using:

$$T = \begin{bmatrix} 1 & \mathbf{0}^T \\ \mathbf{0} & -I_3 \end{bmatrix} \in \mathbf{R}^{4 \times 4}. \quad (52)$$

8 Appendix E: Gradient Compute Ratio

Table 5: Compute-time ratio between Dojo’s gradient and simulation-step evaluations for a variety of robots. We compute the engine’s implicit gradient with respect to the initial configuration, velocity and control input. For a large system like Atlas, using a finite-difference (FD) scheme to evaluate the dynamics Jacobian in maximal coordinates would require at least 400 simulation-step evaluations. Alternatively, Dojo computes this Jacobian at the cost of approximately 4 simulation-step evaluations: a potential 100 times speedup on a single thread.

	Atlas	humanoid	quadruped	ant	half-cheetah
Dojo	3.7	4.9	2.5	2.3	1.2
FD	472.6	194.7	170.3	197.0	94.8

Appendix F: Energy and Momentum Conservation

An accurate robotics simulator conserves important physical quantities like energy and momentum. Following the methodology from [35], we simulate “astronaut,” a free-floating humanoid, and measure the drift of these quantities (Fig. 9).

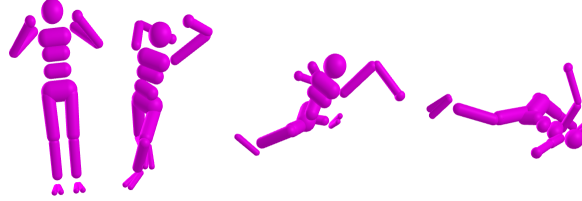


Figure 8: Astronaut simulation for energy and momentum conservation test. Joints are initialized with zero velocities and randomly actuated for 1 second. The simulation is visualized, from left to right.

There is no internal damping or springs, joint limits, or contact, and gravity is turned off. The astronaut is initialized with no linear or angular velocity and momentum drift is computed after one second of uniformly sampled actuation: $u \sim \mathcal{U}(0, 0.05)$. Energy drift is computed over a 100 second period after 1 second of random actuation. MuJoCo exhibits drift in all scenarios. Characteristic of its variational integrator, Dojo conserves both linear and angular momentum to machine precision. Energy does not drift for Dojo but exhibits small bounded oscillations that decrease in amplitude as the time step decreases (Fig. 9). Conservation of energy to machine precision with variational integrators is possible and is a topic of current research [36].

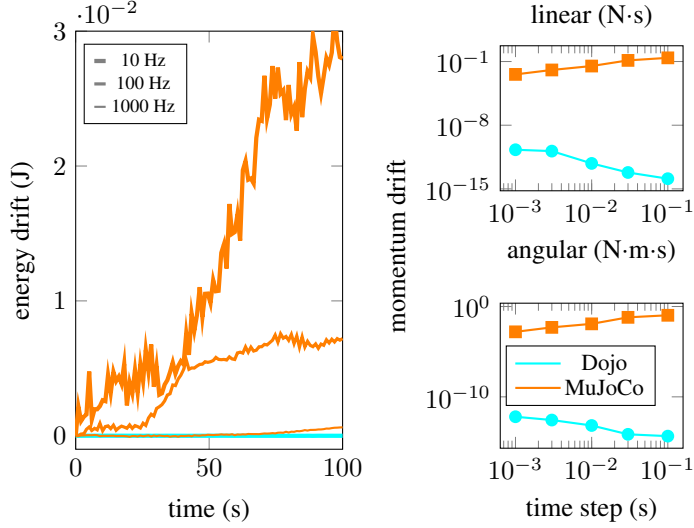


Figure 9: Energy and momentum conservation comparison between MuJoCo and Dojo for the astronaut simulation (Fig 8) using time steps ranging from 0.001 to 0.1 second. Momentum drift is measured after actuating the astronaut for 1 second with random controls. Energy drift is measured over a 100 second simulation after 1 second of random actuation. Dojo achieves drift values near machine precision and is insensitive to large time steps.

Appendix G: Trajectory Optimization

Cart-pole. This classic system [37] with two degrees-of-freedom and one control input is tasked with performing a swing-up over a planning horizon $T = 26$ with time step $h = 0.1$. The pendulum starts in the downward position and the controls are initialized with random values. Quadratic costs are used to penalize control effort and displacement from the goal state. The optimizer finds similar swing-up trajectories.

Box. Inputs are optimized to move a stationary rigid body that is resting on a flat surface (Fig. 2) to a goal location that is either to the right or up in the air 1 meter. The planning horizon is 1 second and the controls are initialized with zeros. Dojo uses a time step $h = 0.1$, whereas MuJoCo uses $h = 0.01$ to prevent significant contact violations with the floor. MuJoCo fails in the scenario with the goal in the air, while Dojo succeeds at both tasks.

Hopper. The robot [38] with $m = 3$ controls and $n = 14$ degrees-of-freedom is tasked with moving to a target pose over 1 second. Similar, although not identical, models and costs are used. Dojo uses a time step $h = 0.05$ whereas MuJoCo uses $h = 0.01$. The hopper is initialized with controls that maintain its standing configuration. Quadratic costs are used to penalize control effort and displacement from an intermediate state in the air and the goal pose. The optimizer typically finds a single-hop motion.

Quadruped. The system with $m = 12$ controls and $n = 36$ degrees-of-freedom is tasked with moving to a goal location over a planning horizon $T = 41$ with time step $h = 0.05$. Controls are initialized to compensate for gravity and there are costs on tracking a target kinematic gait and control inputs. The optimizer finds a dynamically feasible motion that closely tracks the kinematic plan.

In addition to optimizing in the maximal-coordinates space, we also transform this state to a minimal representation for comparison. Gradients are computed with $\kappa = 3e-4$.

Appendix H: Reinforcement Learning

Half-cheetah. This planar system with $m = 6$ controls and $n = 18$ degrees-of-freedom is rewarded for forward velocity and penalized for control effort over a horizon $T = 80$ with time step $h = 0.05$.

Ant. The system has $m = 8$ controls and $n = 28$ degrees-of-freedom and is rewarded for forward motion and staying alive and is penalized for control effort and contact over a horizon $T = 150$ with time step $h = 0.05$.

The Gym environments use MuJoCo with time steps $h = 0.01$, since larger steps result in significant interpenetration of the robots with the floor. In contrast, Dojo is able to train reliably in environments with hard contact using a larger time step $h = 0.05$. Training is performed for a fixed number of steps and the policy is compared over the 3 best out of 5 runs for different random seeds. Gradients are computed with $\kappa = 3e-4$.

Appendix I: System Identification

The parameters are learned by minimizing the following loss:

$$\mathcal{L}(\mathcal{D}, \theta) = \sum_{Z \in \mathcal{D}} L(Z, \theta) = \sum_{Z \in \mathcal{D}} \frac{1}{2} \|\mathbf{Dojo}(z_-, z; \theta) - z_+\|_W^2, \quad (53)$$

where $\|\cdot\|_W$ is a weighted norm, which aims to minimize the difference between the ground-truth trajectories and physics-engine predictions. We use a Gauss-Newton method that utilizes gradients:

$$\frac{\partial L}{\partial \theta} = \frac{\partial \mathbf{Dojo}^T}{\partial \theta} W (\mathbf{Dojo}(z_-, z; \theta) - z_+), \quad (54)$$

and approximate Hessians:

$$\frac{\partial^2 L}{\partial \theta^2} \approx \frac{\partial \mathbf{Dojo}^T}{\partial \theta} W \frac{\partial \mathbf{Dojo}}{\partial \theta}. \quad (55)$$

Gradients are computed with $\kappa = 3e-4$.